NANOMETER RESOLUTION TRACKING AND MODELING OF BIDIRECTIONAL AXONAL CARGO TRANSPORT

Minhua Qiu[1,3], Hao-Chih Lee[1,3], and Ge Yang[1,2,3]

[1]Department of Biomedical Engineering, [2]Lane Center for Computational Biology, [3]Center for Bioimage Informatics, Carnegie Mellon University, Pittsburgh, PA, USA

ABSTRACT

Survival and function of neurons depend critically on bidirectional transport of essential cargoes within their axons. To study related molecular mechanisms, we developed an automated single particle tracking method that combines nanometer resolution detection of cargo positions with kymograph-based multiple hypothesis tracking of cargo motion for precise and complete recovery of cargo trajectories. Experiments confirmed that the method can precisely track vesicles in dense axonal traffic of Drosophila motor neurons at 10~20 nm resolution and reliably resolve their trajectories in events of crossing, merging, and splitting. Recovered cargo trajectories were statistically analyzed to identify motion patterns and computationally represented using hidden Markov models to characterize behavior changes. Together, these tools allowed us to reliably detect and measure subtle changes in dynamics of axonal transport and to discover previously unknown axonal transport properties.

Index Terms— axonal transport, single particle tracking, kymograph, fluorescence imaging, image analysis

1. INTRODUCTION

A hallmark of neurons is their long and thin axons, which in humans can extend for more than one meter at a diameter of a few micrometers. Because of this distributed structure, a wide variety of cargoes essential to the survival and function of neurons must be transported bidirectionally between the neuronal cell body and the synaptic terminal [1]. Transport defects play important roles in the development of many human neurodegenerative diseases such as Alzheimer's disease [2]. Long-distance cargo transport is driven by molecular motor protein kinesin and dynein, which walk nanometer size steps [3]. To characterize the transport process with high precision and sensitivity, we developed an automated single particle tracking technique to recover cargo trajectories at nanometer resolution and computational models to describe cargo behavior. We used these tools to analyze transport of different cargoes in neurons of Drosophila (Fig. 1A), an organism that has been used to model many human neurodegenerative diseases.

Specifically, our cargo tracking technique relies on generating a spatial-temporal cargo movement map, which is often called a kymograph (Fig. 1B). Different kymograph-based approaches for tracking axonal cargo transport have been reported previously [4, 5]. However, these approaches have important limitations in the information that can be recovered and in their resolution and robustness. The method developed in this study overcomes such limitations. First, previously reported approaches cannot recover lateral movement of cargoes, which are oblique or perpendicular to the direction of axon extension. Recovering this information is essential to characterizing transport driven by dynein because lateral movement is a fundamental aspect of its stepping behavior [6]. We achieved this goal by combining a spline-based 2D representation of cargo movement with nanometer resolution tracking of cargo motion. Second, the reported approaches have limited resolution. We achieved nanometer tracking resolution by using nanometer resolution detected cargo positions to refine estimated cargo positions recovered from kymograph-based tracking. Finally, the reported techniques rely on empirical rules to link detected cargo trajectory fragments into full trajectories. We found such rules to have limited robustness in resolving dense axonal cargo traffic in which cargoes frequently cross, merge, and split. We used a general and flexible multiple hypothesis tracking technique that automatically recovers full trajectories from trajectory fragments and reliably resolves cargo movement in events of cargo crossing, merging, and splitting.

After recovery of complete cargo trajectories, cargo movement can be characterized by calculating motion metrics such as velocity and run-length. However, these metrics are limited in representing cargo behavior. For example, they cannot directly describe cargo behavior patterns. To overcome this limitation, we statistically analyzed velocities of cargo movement and identified different velocity modes. We then described temporal cargo behavior using hidden Markov models [7, 8], which provide optimal estimations of the state of individual cargoes at each time and the transition probabilities between different states.

The tools developed in this study have been applied in several axonal transport studies, e.g. [9]. In addition to axonal transport, these tools can also be used to study other axon-based motility processes of neuronal cells as well as one-dimensional intracellular transport processes in non-neuronal cells. For example, the nanometer resolution particle tracking technique developed in this study has been used to analyze movement of motor protein kinesin-5 on individual microtubules [10].

2. IMAGE DATA COLLECTION

Axonal transport of vesicles carrying amyloid precursor protein tagged with YFP (APP-YFP) or synaptotagmin tagged with GFP (SYN-GFP) were imaged in axons within segmental nerves of dissected Drosophila 3rd instar larvae. Expression of UAS-APP-YFP and UAS-SYN-GFP was confined to only a few axons by using the SG26.1 GAL4 driver line. Axonal transport was analyzed under different genetic backgrounds, including various genetic mutations of kinesin and dynein subunits. Specifically, Drosophila 3rd instar larvae were dissected in Ca^{2+}-free medium consisting of NaCl (128mM), EGTA (1mM), $MgCl_2$ (4mM), KCl (2mM), HEPES (5mM), and sucrose (36mM). Dissected larvae were inverted and pressed onto a cover slip. Axons with fluorescently labeled vesicles were identified and imaged on a

Nikon Eclipse Ti-E inverted microscope with a Photometric CoolSnap HQ2 camera and a 100×/1.41 NA oil objective lens. For each animal, a total of four regions (A3-6) marked by denticle bands and separated at ~500 μm spacing along the same axon were imaged (Fig. 1A). Movies were collected for 20 seconds at 11 frames per second under the control of Nikon Element software.

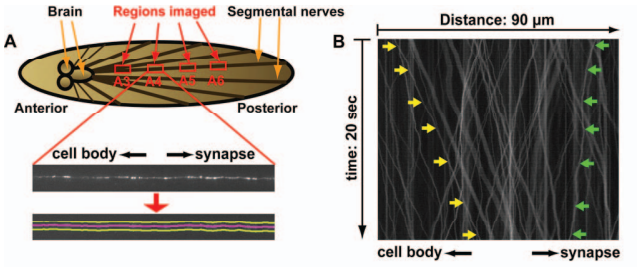


Figure 1. Imaging axonal cargo transport in Drosophila. (A) Upper: regions selected for imaging. Middle: one frame from a time lapse video of vesicle transport. Lower: a band (5 pixels between yellow curves) following the axon (marked in magenta) is taken from each frame (see Section 3.3 for further details). (B) Bands from all frames placed sequentially to generate a kymograph. Yellow and green arrows point to traces of two vesicles moving towards the synapse and the cell body, respectively.

3. IMAGE DATA ANALYSIS

The procedure to recover complete cargo trajectories consists of four steps. First, to determine position and geometry of the axon, a smooth cubic spline is computed through a weighted least-square fitting of all cargo positions from all frames. Second, positions of individual cargoes are detected up to a resolution of 10~20 nanometers by fitting with single or multiple Gaussian kernels representing the microscope point spread function (PSF). Third, a kymograph of cargo movement is generated based on the spline representation of the axon. Cargo trajectories are recovered first by curve detection in the kymograph. A subsequent multiple hypothesis tracking procedure based on global optimization of trajectory smoothness is used to connect detected trajectory fragments into complete trajectories. Recovered trajectories provide estimated positions of cargoes over time. Finally, estimated cargo positions from recovered trajectories are refined using their nearest nanometer resolution detected positions for improved resolution. After recovery of complete cargo trajectories, cargo velocities are analyzed using model-based clustering to identify potential velocity patterns. Hidden Markov models are used to describe temporal cargo behavior and to provide optimal estimation of states and state transition probabilities of individual cargoes.

3.1. Axon detection and representation (Step 1)

Individual frames I_i from a time-lapse video of axonal transport are added together to generate a sum image I_{sum} (Fig. 2A). Since different cargoes move in different regions of the axon over time, adding their images together generates a thin cover that traces the axon. Position and geometry of the axon were detected using the curvilinear feature detector described in [11], which returns a series of axon position coordinates $\left(x^k, y^k\right)_{k=1..M}$ at sub-pixel resolution. A smooth cubic spline f_{axon} was determined by a weighted least squares fitting of $\left(x^k, y^k\right)_{k=1..M}$, i.e. $f_{axon} = \arg\min_f w\sum_{k=1}^{M}\left|y^k - f\left(x^k\right)\right|^2 + (1-w)\int\left|D^2 f(t)\right|^2 dt$, where w is a smoothing weight factor, $0 \le w \le 1$, and $D^2 f$ is the second order derivative of f. After f_{axon} is determined, the coordinate (u,v) of each cargo P in the image plane can be transformed into its coordinate (s,t) along the axon. Let P' denote the minimal distance projection of P onto f_{axon} (Fig. 2B). If $P'P$ forms a positive angle with the positive direction of arc length, $t = +d$, otherwise $t = -d$. Here s is the arc length between P' and the origin, and d is the distance between P and P'. Using this 2D coordinate system is essential to recovering lateral cargo movement.

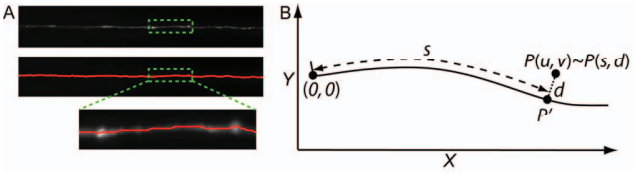


Figure 2. Axon detection and representation. (A) Upper: the sum image. Middle: spline representation of the axon. Lower: a magnified view of the green dotted region. (B) Definition of the arc-length based coordinate system.

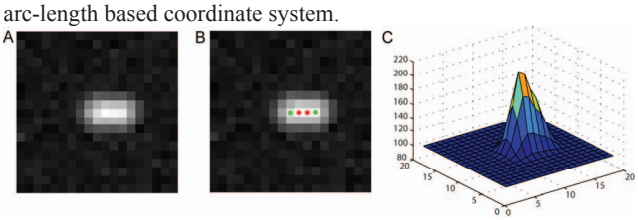


Figure 3. Detection of cargoes in aggregates using multi Gaussian kernel fitting. (A) A synthetic image of two particles. (B) Red dots: initial pixel-level estimations of cargo positions; Green dots: final sub-pixel-level estimation of cargo positions. (C) The mixture of two kernels for optimal sub-pixel resolution fitting.

3.2 Nanometer resolution particle detection (Step 2)

Cargo positions were detected first at pixel resolution by searching for local intensity maxima that are statistically significantly higher than their local background (Fig. 3A-B). Each identified local intensity maximum was fitted by a Gaussian kernel, which was then subtracted from the image. The normalized kernel variance is defined by $\sigma = 0.21\lambda / NA$ where λ is the emission wavelength and NA is the numerical aperture of the microscope objective lens. After the first subtraction, the intensity maximum of the residual signal was located and an additional kernel was fitted and then subtracted. This process was repeated until the optimal number of kernels was determined by minimizing the Bayesian Information Criterion (BIC). Limiting the initial particle detection to pixel level resolution reduces computational cost. Detected pixel-level particle locations were used to initialize a nonlinear optimal fitting using MATLAB function *lsqnonlin* to detect particle locations at sub-pixel resolution (Fig. 3B-C).

3.3 Recovery of complete particle trajectories (Step 3)

Particle tracking starts with generating a kymograph. A regular grid along the spline is generated at a spacing of 1 in arc length. A pixel band of width $2W+1$ following the spline is then computed (Fig. 1A bottom panel). The half width W is chosen to ensure lateral movement of cargo does not exceed this band. Individual pixels are computed by bilinear interpolation in the direction perpendicular to the spline at each individual grid location. After calculating the pixel band for each frame, these bands are placed sequentially to form a kymograph (Fig. 4A).

In the kymograph, the trajectory of each cargo is represented by a curve. Recovery of cargo trajectory starts with detecting such curves using the curvilinear feature detection technique described in [11] (Fig. 4A-B). Individual detected curve positions are then linked. A conservative strategy is adopted to avoid linking error. Consequently, this results in many trajectory fragments (Fig. 4B). Each fragment is used as a seed for linking with other fragments through a multiple hypothesis tracking approach [12], in which different options of linking such fragments are preserved until enough evidence is accumulated for decision making. To limit the size of each hypothesis tracking tree, only the top N (N=32 in this study) candidates with the least overall variations in cargo velocity and intensity are preserved. The final trajectory is chosen from candidates in each tree with the least overall variation (Fig. 4C). Finally, fragments that the automated process fails to link are manually evaluated and connected if possible (Fig. 4D).

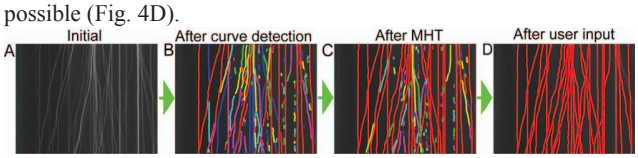


Figure 4. Recovering complete cargo trajectories. (A) Initial kymograph. (B) Some complete trajectories (red) can be recovered after curve detection. But many fragments (varied colors) remain. (C) Multiple hypothesis tracking recovers more complete trajectories. (D) Manual tracing recovers remaining complete trajectories while excluding isolated trajectory fragments.

3.4 Cargo trajectory refinement (Step 4)

Recovered complete cargo trajectories from the kymograph provide estimated cargo positions. Such estimations are refined using nanometer-resolution detected cargo positions through a nearest neighbor search within a region that is empirically determined to be 200nm in radius. For a cargo in the k^{th} frame whose Cartesian image coordinate is (u,v), its arc length coordinate (s,t) can be determined as described in Section 3.1. Its coordinate in the kymograph plane is defined by $(s,(k-1)(2W+1)+W+t+0.5)$. Because of the one-to-one correspondence between cargo image coordinate and kymograph coordinate, the original cargo position in the image plane can be directly determined. When multiple candidates are available within the search region, often due to cargo crossing, merging, and splitting, cargo positions before and after the position are also used to resolve conflicts.

3.5 Statistical analysis of cargo behavior

Velocities of individual cargoes were calculated from their trajectories. Using model-based clustering, we determined that cargo velocity follows three different modes (Fig. 5A). To estimate the transition probabilities between each modes, we described cargo behavior using Hidden Markov models [7, 8] in which each state corresponds to a cargo velocity mode. Different levels of details can be chosen in modeling. We used the coarse model shown in Fig. 5B to determine the transition probabilities of cargo between pause (P) and anterograde (A, i.e. towards synapse) movement and retrograde (R, i.e. towards cell body) movement. A finer scale model (Fig. 5C) allows us to determine the transition probability between e.g. different anterograde velocity modes. The HMM framework not only allows to estimate the transition probabilities but also to optimal classify the state of individual cargoes at each instant by using e.g. the Viterbi algorithm. All computation was performed using the PMTK (Probabilistic Modeling Toolkit for MATLAB/Octave) package.

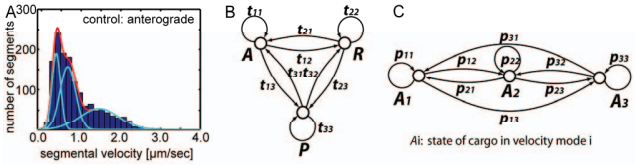


Figure 5. Statistical analysis and modeling of cargo behavior. (A) Anterograde vesicle velocity follows three modes (cyan). (B) A coarse model of state transition between anterograde movement, retrograde movement, and pause. (D) State transition model between different anterograde velocity modes.

4. RESULTS

4.1 Performance of particle detection

To test performance of our particle detection technique, fluorescent beads were rigidly mounted onto a glass slide anchored on a MCL Nano-BioS200 nanopositioning stage. The stage was controlled to move at 8nm, 16nm, and 24nm steps to match with reported step sizes of kinesin and dynein. Actual bead positions (i.e. ground truth) were read from the stage capacitance sensor and compared to software reported bead positions. Under 8nm, 16nm, 24nm step sizes, the detection errors are -0.0±4.4nm (mean ± standard deviation; n = 100), -0.1±4.8nm (Fig. 6A; n = 100), and 0.1±5.9nm (Fig. 6B; n = 100), respectively. The increase in estimation error standard deviation was caused by an increase in stage vibration under increasing step sizes. Overall, our detection technique can achieve a resolution of ~10-20 nm. Detection resolution for particles in aggregates was tested through computer generated synthetic images. Under an SNR of 5-10 that is typical of actual experiments, our algorithm can reliably resolve particles at ~120 nm apart. Higher SNR allows better resolution.

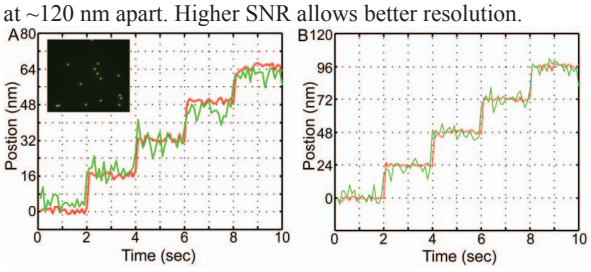


Figure 6. Particle detection resolution. (A) Software reported particle position (green) versus actual particle position (red) at 16 nm steps. Inset: a sample image of the fluorescence beads used. (B) Same comparison at 24 nm steps.

4.2 Performance of particle tracking

More than two thousand movies were fully analyzed in the development of the particle tracking method. In an experiment

to quantify the tracking performance, 40 videos were analyzed manually through kymograph curve tracing followed by location refinement to produce ground truth. Our particle tracking technique recovered ~30% of complete cargo trajectories after initial curve detection (Fig. 4A-B). After multiple hypothesis tracking, the recovery rate was increased to ~70% (Fig. 4C). Detailed analysis was also performed on individual trajectories, which determined the average trajectory coverage rate to be >95% and the worst-case trajectory deviation to be less than 100nm.

4.3 Comparison of cargo transport in healthy versus degenerative neurons

We used the computational tools to analyze cargo movement in healthy as well as degenerative neurons with modifications of kinesin (*khc*^{8}/+) and dynein (*dhc64c*$^{4\text{-}19}$/+ & *GEN-DIC*/+). We found that anterograde (i.e. towards synapse) cargo velocity follows three modes that approximately satisfy a ratio of 1:2:4 (Table 1). However, contributions (i.e. probabilities) of individual modes shift in mutants. Using HMM, we found that state transition probabilities also change under different genetic modifications.

Table 1. Cargo velocity modes (unit: μm/sec) in healthy (*wt*) versus degenerative neurons. *: mode center; ^: mode probability

	Mode I		Mode II		Mode III	
wt	0.37*	26%^	0.66	39%	1.46	35%
***khc*^{8}/+**	0.38	55%	0.75	32%	1.36	13%
***dhc64c*$^{4\text{-}19}$/+**	0.42	36%	0.69	27%	1.60	36%

Table 2. Cargo state transition probabilities in healthy (*wt*) versus degenerative neurons, where $P_1 = p_{11} + p_{22} + p_{33}$ (Fig. 5C) is the probability of no mode change, $P_2 = p_{12} + p_{21} + p_{23} + p_{32}$ is the probability of shifting to neighboring states (i.e. $I \leftrightarrow II$, $II \leftrightarrow III$) and $P_3 = p_{13} + p_{31}$ is the probability of mode jump (i.e. $I \leftrightarrow III$).

	P_1	P_2	P_3
wt	0.59	0.38	0.03
***khc*^{8}/+**	0.79	0.20	0.01
***GEN-DIC*/+**	0.79	0.18	0.03

5. DISCUSSION

In this study we developed computational tools for tracking and modeling bidirectional axonal cargo transport in neurons. Using these tools, we found that axonal cargoes follow multiple velocity modes in their movement and switch frequently between these modes. These properties were previously unknown and provide important insights into the molecular mechanisms of axonal transport [9]. The particle tracking technique developed in this study overcomes several important limitations of previously reported approaches. In particular, it can precisely track at nanometer resolution both longitudinal and lateral cargo movement and can reliably resolve cargo trajectories from complex dynamic events involving cargo crossing, merging, and splitting. The statistical analysis and computational models of this study characterize cargo movement at a behavior rather than trajectory level and can identify inherent patterns of cargo movement. Furthermore, these computational tools can be used to study not only axonal transport but also a broad range of other intracellular processes of one-dimensional movement along cytoskeletal filaments.

This study has several limitations, which are being addressed in our ongoing research. To achieve a 90% or higher success rate in automated recovery of complete cargo trajectories, we are incorporating concepts and techniques of machine learning and perceptual organization into the multiple hypothesis tracking framework currently used. To achieve a significantly higher (i.e. 10-20nm) level resolution in resolving individual cargoes within aggregates, we are using super-resolution imaging techniques, specifically STORM (stochastic optical reconstruction microscopy).

ACKNOWLEDGEMENTS

This study was supported in part by an ICES-DOWD Fellowship (M.Q.), a grant from the Samuel and Emma Winters Foundation (G.Y.), and grants MCB-1052660 and DBI-1052925 from the U.S. National Science Foundation (G.Y.).

REFERENCES

[1] A. Brown, "Axonal transport of membranous and nonmembranous cargoes: a unified perspective," *J. Cell Biol.,* vol. 160, no. 6, pp. 817-821, 2003.

[2] K. J. De Vos, A. J. Grierson, S. Ackerley *et al.*, "Role of axonal transport in neurodegenerative diseases," *Annual Review of Neuroscience,* vol. 31, no. 1, pp. 151-173, 2008.

[3] R. D. Vale, "The molecular motor toolbox for intracellular transport," *Cell,* vol. 112, no. 4, pp. 467-480, 2003.

[4] K. Zhang, Y. Osakada, W. Xie *et al.*, "Automated image analysis for tracking cargo transport in axons," *Microscopy Research and Technique,* vol. 74, no. 7, pp. 605-613, 2010.

[5] A. Mukherjee, B. Jenkins, C. Fang *et al.*, "Automated kymograph analysis for profiling axonal transport of secretory granules," *Medical Image Analysis,* vol. 15, no. 3, pp. 354-367, 2011.

[6] S. L. Reck-Peterson, A. Yildiz, A. P. Carter *et al.*, "Single-molecule analysis of dynein processivity and stepping behavior," *Cell,* vol. 126, no. 2, pp. 335-348, 2006.

[7] L. R. Rabiner, "A tutorial on hidden Markov models and selected applications in speech recognition," *Proc. IEEE,* vol. 77, no. 2, pp. 257-286, 1989.

[8] R. Das, C. W. Cairo, and D. Coombs, "A hidden Markov model for single particle tracks quantifies dynamic interactions between LFA-1 and the actin cytoskeleton," *PLoS Comput Biol,* vol. 5, no. 11, pp. e1000556, 2009.

[9] G. F. Reis, G. Yang, L. Szpankowski *et al.*, "Molecular motor function in axonal transport in vivo probed by genetic and computational analysis in Drosophila," *Molecular Biology of the Cell*, to appear.

[10] J. S. Weinger, M. Qiu, G. Yang *et al.*, "A nonmotor microtubule binding site in kinesin-5 is required for filament crosslinking and sliding," *Current Biology,* vol. 21, no. 2, pp. 154-160, 2011.

[11] C. Steger, "An unbiased detector of curvilinear structures," *IEEE Trans. PAMI,* vol. 20, no. 2, pp. 113-125, 1998.

[12] S. Blackman, and R. Popoli, *Design and Analysis of Modern Tracking Systems*: Artech House, 1999.